

Rethinking Normalization Strategies and Convolutional Kernels for Multimodal Image Fusion

Dan He^{1,*} Guofen Wang^{2,*} Weisheng Li^{1,†} Yucheng Shu^{1,†} Wenbo Li¹
Lijian Yang¹ Yuping Huang¹ Feiyan Li¹

¹ Chongqing University of Posts and Telecommunications ² Chongqing Normal University
d230201011@stu.cqupt.edu.cn

Abstract

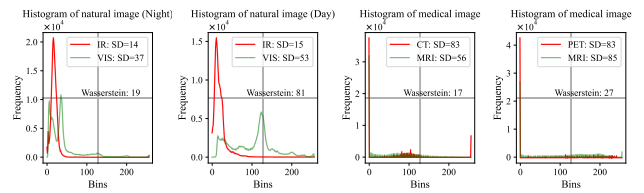
Multimodal image fusion (MMIF) aims to integrate information from different modalities to obtain a comprehensive image, aiding downstream tasks. However, existing methods tend to prioritize natural image fusion and focus on information complementary and network training strategies. They ignore the essential distinction between natural and medical image fusion and the influence of underlying components. This paper dissects the significant differences between the two tasks regarding fusion goals, statistical properties, and data distribution. Based on this, we rethink the suitability of the normalization strategy and convolutional kernels for end-to-end MMIF. Specifically, this paper proposes a mixture of instance normalization and group normalization to preserve sample independence and reinforce intrinsic feature correlation. This strategy promotes the potential of enriching feature maps, thus boosting fusion performance. To this end, we further introduce the large kernel convolution, effectively expanding receptive fields and enhancing the preservation of image detail. Moreover, the proposed multipath adaptive fusion module recalibrates the decoder input with features of various scales and receptive fields, ensuring the transmission of crucial information. Extensive experiments demonstrate that our method exhibits state-of-the-art performance in multiple fusion tasks and significantly improves downstream applications. The code is available at <https://github.com/HeDan-11/LKC-FUNet>.

1. Introduction

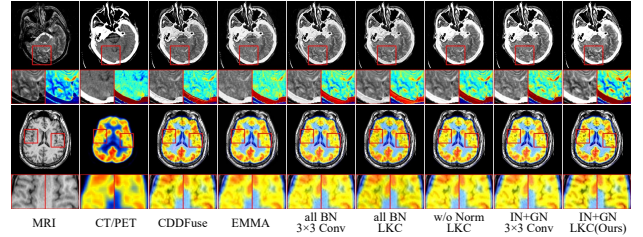
In reality, single-modal images capture limited information and each modality contains essentially different information [9]. Image fusion technology fully integrates the complementary information of different modalities to gen-

*These authors contributed equally

†Corresponding author



(a) Histogram analysis of varied images. SD: standard deviation.



(b) Impact of diverse normalization methods and large kernel convolution (LKC) on fusion performance.

Figure 1. Evaluating pixel intensity distribution discrepancies and fusion results exhibition.

erate a comprehensive representation of the image [52]. It is widely used for scene information enhancement or restoration [23, 24, 51]. Moreover, object detection [59, 60] and semantic segmentation [25, 27] can also benefit from clearer representations of scenes and objects in the fused images [61]. Fusion tasks include infrared and visible image fusion (IVIF)[18, 47], medical image fusion (MIF) [29, 34], multi-exposure image fusion [19], and so on, where IVIF and MIF are very similar and challenging subcategories [40]. Specifically, in IVIF, fused images can avoid the drawbacks of visible (VIS) images that are sensitive to illumination conditions and infrared (IR) images that are noisy and low resolution [24, 63]. Similarly, MIF generates images that comprehensively reflect the information of tissues, organs, and metabolism to assist medical diagnosis and improve reliability [55].

In recent years, many deep learning methods [32, 38, 50, 56, 58, 64] have been developed to address challenges in image fusion. Common encoder-decoder models demonstrat-

ing promising results utilize convolutional neural networks (CNNs) [54, 57] and Transformer [21, 33, 65] to extract features and reconstruct images. It has achieved relatively satisfactory convergence performance in IVIF. However, it has focused more on the improvement of objective indicators in MIF, without sufficiently considering the needs of MIF itself. In fact, there are the following significant differences between IVIF and MIF: 1) Fusion goals: IVIF emphasizes the overall structure and salient objects. Whereas in MIF, details and structural information must be fully retained, and tiny textures may indicate important lesion information. 2) Data distribution. Fig. 1a shows that IR and VIS images are Gaussian distributed, while medical images are highly sparsely distributed. 3) Statistical properties. Medical images possess more complex details, and their statistical values, such as average gradient (AG), spatial frequency (SF), and standard deviation (SD), are far higher than those of IR and VIS images. 4) Intra-task inter-sample differences. Fig. 1a shows that the pixel distributions of VIS images differ significantly between daytime and nighttime scenes. Meanwhile, computed tomography (CT) images have more high-brightness regions compared to magnetic resonance imaging (MRI) and positron emission tomography (PET) images, which might result in mutual interference during the fusion process.

Some methods [5, 63] are trained to achieve only unified fusion on IR and VIS images. These methods attain excellent performance in IVIF but severe sacrifice of details in medical images, clearly overlooking differences 1-3. SDNet [54] and CDDFuse [61] are trained with different parameters to deal with the two tasks. Nevertheless, the emphasis continues to be on IVIF, while for MIF, only its model parameters are adjusted. This neglects the limited effective feature and the strict fusion requirements for detail retention in MIF and fails to solve the conflict between simultaneously retaining the high-brightness regions in CT/functional images and the detail information in MRI. We aim to rethink the fitness of the underlying components in this discrepancy case and design suitable models to resolve fusion conflicts and reduce inter-sample interference during training.

Firstly, early fusion frameworks [8, 57] are derived from advanced vision tasks, in which the employed batch normalization (BN) seeks to normalize the feature distribution across the entire batch; but this approach ignored the independence of samples, leading to data smoothing. This has less impact on IVIF which emphasizes structure preservation. However, for medical images that are highly sparsely distributed and require strict detail retention, the interaction between samples will also cause a conflict between regions of high brightness and detail retention. While some methods [5, 12, 14, 25] forgo normalization to preserve sample independence, they fail to account for the inherent proper-

ties of images and the intrinsic relationships between features, resulting in limited improvements in fusion performance. Secondly, large kernel convolution (LKC) can capture spatial information within a wider range and is crucial for preserving image structure and details. However, its exploration in image fusion is limited, which may be related to its performance bottleneck. As depicted in Fig. 1b, when BN is applied, the interaction among samples results in data smoothing, further reducing effective features. Here, the large receptive fields of LKC have a limited or even hindering effect on detail retention. Not using normalization fails to offer better image features and makes it hard to raise the upper limit of fusion performance. Finally, when using UNet [35], simple skip connections do not consider the relative importance of feature maps in different paths during the fusion process. This may result in crucial features being neglected.

To address the above issues, we focus on exploring an efficient UNet to cope with the challenges of substantial differences among tasks and limited feature extraction. We employ a mixture of IN and GN to fully consider the sample independence, image properties, and intrinsic connections among features. This strategy enhances the generation of rich feature maps while more effectively preserving the distinctive attributes of source image pairs, as illustrated in Fig. 1b. The strategy elevates the upper bound of fusion performance, at this point, the application of LKC enhances detail retention capabilities. Finally, the feature maps in the input decoder are recalibrated by combining spatial, channel attention, and bidirectional interactions. We fully consider four critical differences, thereby guaranteeing not only outstanding performance in MIF, but also full applicability to IVIF. Our contributions are summarized as follows:

- A UNet with LKC is proposed to achieve multimodal image fusion (MMIF), namely LKC-FUNet, including IVIF and MIF.
- Rethink the impact of normalization and LKC on image fusion. Verify the inappropriateness of BN in MMIF. Mixing IN and GN preserves image properties and is well suited for highly sparsely distributed fusion tasks. Under the above strategy, LKC enlarges the "effective receptive field" to better preserve the detailed information and significantly improve the fusion performance.
- A multipath adaptive fusion module is designed for feature fusion across different receptive fields and at various scales. Spatial-channel dual-attention feature maps, bidirectional interactions, and recalibration are used to provide more comprehensive inputs to the decoder.
- Our method significantly improves multiple metrics in both tasks and achieves breakthroughs in MIF visualization. It is also shown to facilitate downstream multimodal object detection and semantic segmentation.

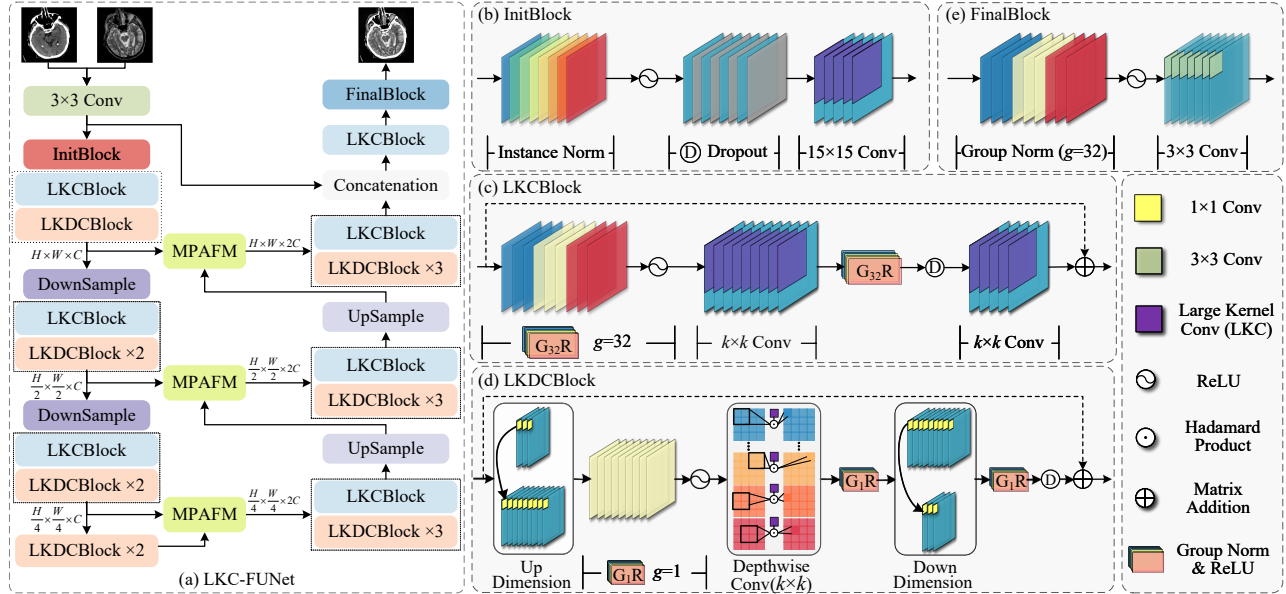


Figure 2. Overall architecture of LKC-FUNet.

2. Related work

Multimodal image fusion. Deep learning methods in MMIF fall into four categories: encoder-decoder models, adversarial models, task- and text-driven models, and other models. Early coder-decoder models [17, 57] utilize pre-trained autoencoders for feature extraction and image reconstruction, emphasizing the design of fusion rules. Later on, it develops into an end-to-end fusion model to get rid of the limitation of manual fusion rules. In this case, it mainly combines CNN and Transformer [33, 41] to enrich the feature representations, and facilitates the modal information interaction through the feature fusion module. Generative Adversarial Network (GAN)-based methods [32, 60] define image fusion as a game between a generator and a discriminator, where texture details are preserved and salient targets are highlighted in the confrontation. However, the instability of training is not effectively addressed. In recent years, studies have focused on the adaptability of fused images to downstream tasks. CDDFuse [61] and EMMA [63] measure the fusion performance in terms of the accuracy of object detection and image segmentation. And some studies [25, 45, 55, 59, 60] enhance the performance by guiding the fusion with semantic information of the downstream tasks. Currently, contrast learning [24, 58] and diffusion model [38, 53, 62] are also introduced into fusion field. In addition, researchers have designed various loss functions [9, 50] based on image fusion characteristics, which provide substantial guidance for network training. Although deep learning-based unified methods have demonstrated strong fusion performance on IVIF, they are often simply migrated to MIF.

Normalization. The normalization technique unifies

the data scale by scaling and panning to avoid the feature value magnitude difference affecting the model training, which makes the neural network have better generalizability [7, 36]. Common BN [13] accelerates training and improves stability. IN [44] and its variant [11] are suitable for image style conversion and synthesis, preserving details of the original image. GN [49] combines the advantages of BN and IN to perform well in image-intensive tasks. BCN [15] adaptively combines channel and batch information to improve classification performance. Although normalization has a significant role in advanced vision tasks, it is rarely applied in image fusion. The fusion results are mainly dependent on the source image pairs and the use of IN and GN is more helpful in preserving the image properties.

Large kernel convolution. LKC obtains more context-rich convolutional features by expanding the receptive field, thus excelling in image classification [22] and segmentation [26]. Among them, LR-Net [10] and ConvNeXt [30] can benefit from 7×7 kernel. However, LR-Net suffers from performance degradation at 9×9 . Performance bottlenecks and parameter spikes limit the kernel to smaller values. To address this challenge, RepLKNet [6] achieves advanced performance by reparameterizing the 31×31 deep convolution. And SLkK [28] extends the kernel size to 51×51 by kernel decomposition and sparse grouping. Although LKC has facilitated performance improvements in many areas, its importance for image fusion remains elusive.

3. Method

3.1. Overview

The proposed method is a UNet architecture as shown in Fig. 2. We splice the source image pairs into the input

model to completely avoid the design of inter-modal fusion rules. The basic modules are the initial block (InitBlock), LKCBLOCK, and Large kernel deep convolutional block (LKDCBLOCK). They are designed according to the following principles: enhance the image properties in the early stage, strengthen the correlation between features in the late stage, and maintain the independence between samples throughout. Finally, a multipath adaptive fusion module (MPAFM) is used to recalibrate the decoder inputs.

3.2. Basic modules

InitBlock. We use IN and LKC with 15×15 as the initial block. Facing two modal image splicing inputs with very different statistical properties, IN targetedly normalizes the properties of each image to significantly reduce the intrinsic differences between modalities, while preserving more detailed features. On the other hand, LKC is more capable of capturing a wide range of spatial information, strengthening the preservation of image structure and contrast. Considering the computational efficiency and the intrinsic relationship between features, GN is adopted for the other modules.

During the fusion process, different regions have different feature requirements, e.g., features should be consistent in the background, while regions with complex structures and details should be as unique as possible. Therefore, we compute the feature map consistency in chunks. This reflects the redundancy within the region and corresponds to the structure of the original map. From Fig. 3, it is reasonable that the consistency of the background regions under BN and IN is high. Moreover, the redundancy of complex regions in IN is significantly lower. This indicates that IN combined with LKC generates a richer feature map, which is beneficial for maintaining the image structure and details.

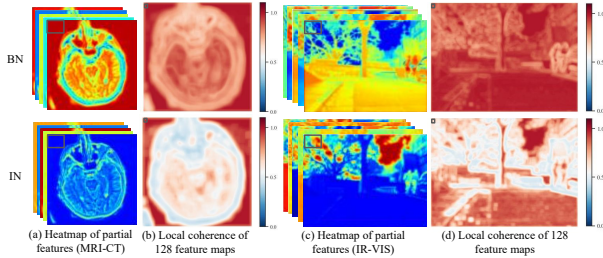


Figure 3. Local consistency of the feature map after InitBlock. Higher values in (b) and (d) indicate more redundant features in the corresponding patches.

LKCBLOCK. Consists of two Blocks containing GN, ReLU, optional Dropout, and convolutional layers. The convolution kernels at different stages are set to 15, 7, 5, and 5 to accommodate the feature extraction needs at different resolutions. Larger convolutional kernels are used for global information capture at high resolution, which helps in understanding the overall structure of the image. While smaller convolutional kernels are used for attention to de-

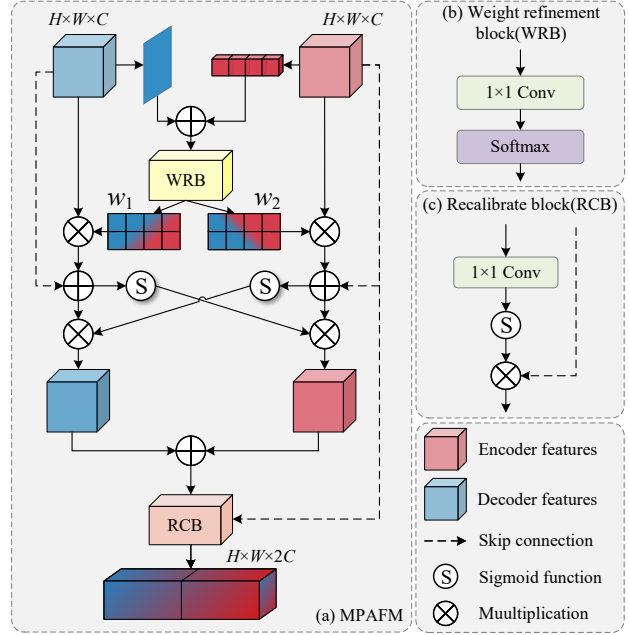


Figure 4. Multipath adaptive fusion module (MPAFM).

tails at low resolution, enhancing the model’s perception of local features. The final residual connection provides a stable gradient flow and preserves the necessary information.

LKDCBLOCK. Considering the efficiency of the model, we use LKDCBLOCK [6] combined with LKCBLOCK. It is worth noting that the grouping of GN in LKDCBLOCK is set to 1. This change is based on the property of deepwise convolution, in which convolution kernels independently operate on corresponding feature maps. At this point, grouping the GN may result in weak connections between features and amplification of certain features.

3.3. Multipath adaptive fusion module

Simple skip connections in UNet do not consider the relative importance of feature maps in different paths during the fusion process, which may result in some important features being overlooked [2, 16, 46]. Therefore, this section proposes the MPAFM to process the feature maps of the corresponding layers of the encoder and decoder, as shown in Fig. 4. The aim is to suppress unimportant features to minimize artifacts while progressively capturing detailed and structural information for the image at different scales and different receptive fields.

Attention feature map. Obtain an attention feature map that integrates spatial and channel information. First, channel attention \mathcal{C} is used to process the encoder’s feature e to reflect the importance of each channel. Spatial attention \mathcal{S} is used to process the decoder’s feature d to capture the important regions. And the weight map that combines the two provides more comprehensive information guidance. Further, the weight map is refined into A and B using the weight refinement block \mathcal{W} . They act on different input

feature maps to enhance important features more precisely. The formula is as follows:

$$A, B = \text{Split}(\mathcal{W}(\mathcal{C}(e) + \mathcal{S}(d))) \quad (1)$$

$$e_{att} = A \odot e \quad (2)$$

$$d_{att} = B \odot d \quad (3)$$

where \odot denotes the dot product operation and *Split* indicates the division operation.

Bidirectional interaction. Realizing the information interaction of the coder-decoder’s attentional feature maps to facilitate complementary feature fusion at different receptive fields and different scales.

$$f = \sigma(e_{att}) \odot d_{att} + \sigma(d_{att}) \odot e_{att} \quad (4)$$

where σ is the sigmoid function.

Recalibration block \mathcal{R} . To generate a pixel attention map that is consistent with the dimensionality of the input image and recalibrate the features of the input decoder. It is ensured that the input feature maps are effectively augmented with details, context-aware information, etc.

$$X = \mathcal{R}(f) \quad (5)$$

3.4. Loss function

The loss function of the fusion network consists of a mixture of structure level, intensity level, and gradient level defined as follows:

$$\mathcal{L}_{total} = \mathcal{L}_{ssim} + \mathcal{L}_{int} + \mathcal{L}_{grad} \quad (6)$$

where $\mathcal{L}_{ssim} = 1 - SSIM(I_A, I_B^Y, I_F)$. SSIM is the structural similarity [48]. In the intensity loss, we want to focus on high-brightness regions, calculated as follows:

$$\mathcal{L}_{int} = \frac{1}{HW} \cdot \|I_F - \max(I_A, I_B^Y)\|_1 \quad (7)$$

where I_A and I_B are the source images, I_B^Y is the luminance channel of I_B , and I_F is the fused image. $\|\cdot\|_1$ denotes the L_1 norm and $\max(\cdot)$ represents the element-wise maximum operation. In the gradient loss, the fused image should be consistent with the strongest details in the source image, i.e:

$$\mathcal{L}_{grad} = \frac{1}{HW} \cdot \| |\nabla I_F| - \max(|\nabla I_A|, |\nabla I_B^Y|) \|_1 \quad (8)$$

where ∇ indicates the gradient operator used for texture information measurement within an image.

4. Experiment

4.1. Medical image fusion

4.1.1. Setup

Datasets. We selected three medical image combinations from the Harvard Medical School website [1] for MIF experiments, including MRI-CT, MRI-PET, and MRI-single-photon emission computed tomography (SPECT) image pairs. We trained on 40 pairs of datasets containing all modalities and then tested on 50 pairs of MRI-CT, MRI-PET, and MRI-SPECT images respectively. All images are aligned and have a size of 256×256 pixels.

Metrics. We quantitatively analyzed the fusion results using six metrics: SD, AG, SF, sum of the correlations of differences (SCD), visual information fidelity for fusion (VIFF), and structural similarity index measure (SSIM). Higher metrics indicate better fusion performance. Detailed information on these metrics can be found in [31].

Comparison methods. We compare the fusion results with five state-of-the-art (SOTA) methods: CDDFuse [61], EMMA [63], MMDRFuse [5], GeSeNet [20] and FATFusion [39]. It is worth noting that GeSeNet and FATFusion are only applied to MIF.

Implementation details. The experimental equipment is a server equipped with four NVIDIA GeForce RTX 3090 GPUs under the PyTorch framework. The images are randomly cropped into 64×64 patches with a batch size of 32 during training. We train the network for 1000 epochs using the Adam optimizer with an initial learning rate of $1e-4$.

4.1.2. Comparison with SOTA methods

Qualitative comparison. Visual comparisons are shown in Fig. 5, containing five representative pairs of medical images. It is obvious that severe detail weakening occurs in CDDFuse, EMMA, MMDRFuse, and GeseNet, while FATFusion completely neglects the preservation of high-brightness regions. Our method not only preserves the details in MRI completely, but also restores the cranial and calcified regions in CT images, and the radiotracer distribution in functional images, which can provide more comprehensive diagnostic information.

Quantitative Comparison. Tab. 1 shows objective results for six metrics. Our method demonstrated excellent performance in almost all metrics. The slightly lower AG and SF resulting from MRI-CT fusion preserving a more complete cranial region is acceptable. In summary, the fusion results obtained by our method are more in line with the needs of MIF.

4.1.3. Ablation experiment

We conducted ablation studies on three medical datasets to verify the proposed method, and the results are presented in Fig. 1b and Tab. 2. Obviously, the performance of models with BN is limited and even shows a regressive tendency

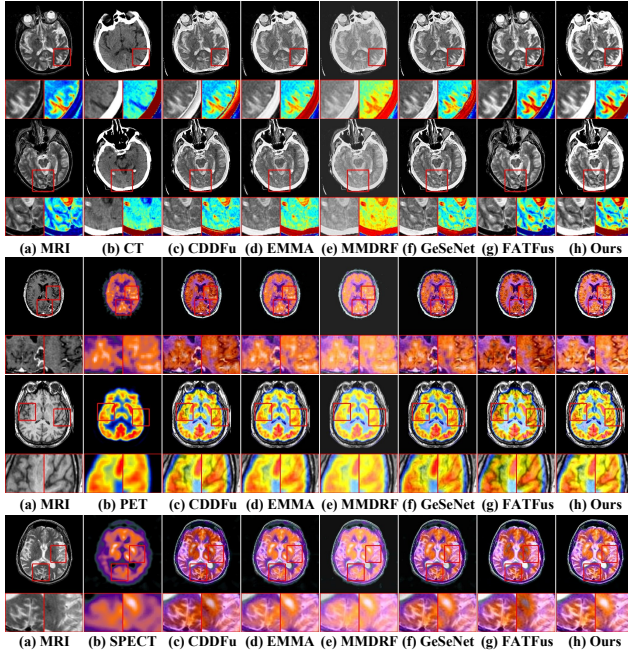


Figure 5. Visual comparison with five SOTA methods in MIF.

Dataset: MRI-CT Image Fusion (50 pairs) [42]						
Methods	SD	AG	SF	SCD	VIFF	SSIM
CDDFu* [61]	84.803	<u>9.292</u>	38.121	1.376	0.413	<u>0.727</u>
EMMA* [63]	<u>86.493</u>	7.534	27.405	<u>1.464</u>	<u>0.421</u>	0.668
MMDRF* [5]	75.768	5.723	22.993	1.263	0.371	0.263
GeSeNet [20]	85.591	9.360	<u>37.552</u>	1.358	0.405	0.529
FATFus [39]	72.680	7.688	26.901	0.906	0.119	0.717
Ours	94.033	8.242	33.836	1.576	0.456	0.731
Dataset: MRI-PET Image Fusion (50 pairs) [42]						
Methods	SD	AG	SF	SCD	VIFF	SSIM
CDDFu* [61]	69.309	8.257	27.883	1.405	0.502	0.739
EMMA* [63]	<u>74.011</u>	7.151	22.547	1.602	<u>0.555</u>	0.668
MMDRF* [5]	71.833	6.131	20.099	<u>1.604</u>	0.539	0.262
GeSeNet [20]	71.110	8.311	27.508	1.470	0.553	0.486
FATFus [39]	69.284	<u>8.760</u>	<u>30.089</u>	1.278	0.402	0.727
Ours	78.345	9.424	31.663	1.660	0.590	<u>0.734</u>
Dataset: MRI-SPECT Image Fusion (50 pairs) [42]						
Methods	SD	AG	SF	SCD	VIFF	SSIM
CDDFu* [61]	66.015	7.364	24.824	1.039	0.521	0.719
EMMA* [63]	68.472	6.378	20.555	1.528	<u>0.606</u>	0.664
MMDRF* [5]	68.655	5.499	18.248	<u>1.597</u>	0.589	0.263
GeSeNet [20]	66.965	7.469	24.686	1.409	0.602	0.490
FATFus [39]	<u>73.948</u>	<u>7.988</u>	<u>27.301</u>	1.431	0.561	0.711
Ours	75.481	8.731	29.770	1.651	0.637	0.723

Table 1. Quantitative comparisons in MIF. Boldface: best, underline: second-best, *: unified image fusion method.

when combined with LKC. IN in the InitBlock is essential for maintaining image properties and then significantly enhancing performance when combined with LKC. MPAFM effectively transmits key features by recalibrating decoder inputs. In summary, IN and GN enhance the performance potential, and LKC and MPAFM facilitate the model to reach the upper limit.

Configurations	SD	AG	SF	SCD	VIFF	SSIM
I all BN+3*3 Conv	76.553	8.146	28.280	1.578	0.548	0.736
II all BN+LKC	73.995	7.282	24.928	1.485	0.517	0.748
III BN+GN+LKC	78.506	8.170	26.516	<u>1.609</u>	0.552	0.746
IV IN+GN+3*3 Conv	79.999	8.520	30.974	1.591	<u>0.571</u>	0.735
V w/o Norm	78.414	7.621	26.807	1.584	0.543	<u>0.747</u>
VI w/o MPAFM	<u>81.203</u>	<u>8.908</u>	<u>32.373</u>	1.535	0.569	0.725
Ours (IN+GN+LKC)	83.294	9.127	33.297	1.652	0.578	0.727

Table 2. Ablation experiment results in the test set of MIF. Boldface: best, underline: second-best.

4.2. Infrared and visible image fusion

4.2.1. Setup

Datasets. We perform comparative experiments on three mainstream datasets: MSRS [37], M³FD[60] and TNO[42]. We trained the model on 1083 pairs of images from MSRS and then evaluated the performance on 361 pairs of test data. In addition, the models are applied to the M³FD and TNO datasets without fine-tuning to verify the generalization performance.

SOTA methods. We compare the fusion results with seven SOAT methods: CDDFuse [61], EMMA [63], MMDRFuse [5], LRRFNet [18], SegMIF [25], DCINN [47] and SHIP [64]. It is worth noting that the latter four methods are only applied to IVIF. The training strategy and evaluation metrics are the same as for MIF.

4.2.2. Comparison with SOTA methods

The qualitative comparisons are presented in Fig. 6, again containing five representative pairs of images. It is evident that our method not only clearly highlights objects in dark areas, but also objects in high-intensity areas. This uniqueness enhances our understanding of the depicted scene. Moreover, as shown in Tab. 3, our method attains the most optimal evaluation metrics in all datasets, confirming its applicability to various environmental conditions and object classes. In summary, the full experimental results demonstrate the ability of LKC-FUNet to simultaneously preserve the integrity of source image features and generate information-rich fused images.

4.2.3. Downstream IVIF applications

In this section, IR images, VIS images, and fused images of SOTA methods are applied to object detection and semantic segmentation to examine the benefits of information fusion for downstream tasks.

Object detection. We conduct experiments on the M³FD dataset [60], which contains 4,200 pairs of IR/VIS images and is divided into training/validation/testing sets in a ratio of 8:1:1. The six categories are people, cars, buses, motorcycles, trucks, and lights. We chose yolov5 [43] as the detector and mAP@0.5 to evaluate the detection performance. During training, the epoch, batch size, optimizer, and initial learning rate are set to 1,000, 128, SGD, and 1e-

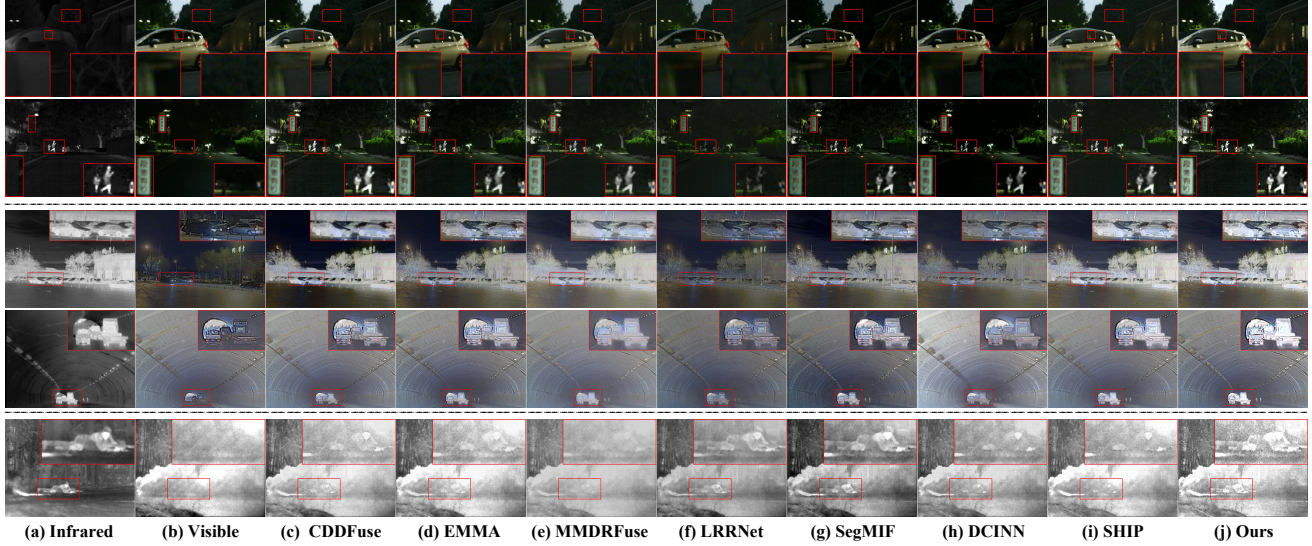


Figure 6. Visual comparison with seven SOAT methods on MSRS, M³FD, and TNO datasets, respectively.

Dataset: MSRS (361 pairs of IR-VIS images) [37]						
Methods	SD	AG	SF	SCD	VIFF	SSIM
CDDFu* [61]	44.570	3.911	11.792	1.754	<u>0.804</u>	<u>0.702</u>
EMMA* [63]	<u>44.578</u>	3.785	11.544	1.629	0.773	0.712
MMDRF* [5]	40.043	3.458	10.345	1.590	0.724	0.692
LRRNet [18]	31.757	2.651	8.464	0.791	0.414	0.614
SegMIF	35.963	3.309	10.417	1.511	0.645	0.573
DCINN [47]	40.112	3.334	10.467	1.478	0.706	0.583
SHIP [64]	41.131	<u>3.933</u>	<u>11.803</u>	1.512	0.701	0.665
Ours	46.574	4.939	15.377	<u>1.682</u>	0.883	0.680
Dataset: M ³ FD (300 pairs of IR-VIS images) [60]						
Methods	SD	AG	SF	SCD	VIFF	SSIM
CDDFu* [61]	38.090	4.569	13.669	1.558	0.540	0.704
EMMA* [63]	38.251	<u>5.340</u>	15.216	1.494	0.491	0.702
MMDRF* [5]	26.594	3.431	10.211	1.471	0.305	<u>0.718</u>
LRRNet [18]	27.179	3.600	10.678	1.463	0.363	0.725
SegMIF	37.929	4.812	14.223	1.751	<u>0.554</u>	0.711
DCINN [47]	44.020	4.303	12.942	0.346	0.319	0.683
SHIP [64]	35.222	5.177	<u>15.247</u>	1.311	0.385	0.693
Ours	40.235	7.414	22.102	1.614	0.671	0.656
Dataset: TNO (37 pairs of IR-VIS images) [42]						
Methods	SD	AG	SF	SCD	VIFF	SSIM
CDDFu* [61]	45.632	4.940	13.313	1.630	0.558	0.682
EMMA* [63]	48.575	<u>5.171</u>	12.646	1.668	<u>0.579</u>	0.661
MMDRF* [5]	28.964	3.037	7.983	1.418	0.261	<u>0.724</u>
LRRNet [18]	42.224	4.104	10.438	1.507	0.415	0.653
SegMIF	<u>46.540</u>	4.916	12.919	1.765	0.550	0.674
DCINN [47]	35.833	3.942	10.433	1.573	0.347	0.725
SHIP [64]	40.149	5.004	<u>13.224</u>	1.455	0.355	0.676
Ours	43.800	6.631	16.713	<u>1.670</u>	0.608	0.636

Table 3. Quantitative comparisons in IVIF. Boldface: best, underline: second-best, *: unified image fusion method.

2 respectively. As shown in Tab. 4, LKC-FUNet has the best detection performance, which indicates that fusing VIS information and highlighting hard-to-observe objects can improve detection accuracy.

Semantic segmentation. We perform semantic seg-

Methods	Peo	Car	Bus	Lam	Mot	Tru	mAP@0.5
IR	86.9	92.9	86.5	78.6	74.9	83.0	83.8
VI	77.3	93.5	87.5	89.5	72.0	79.3	83.2
CDDFu* [61]	86.4	94.2	86.8	88.0	75.4	83.9	85.8
EMMA* [63]	85.8	94.4	86.8	90.3	<u>77.2</u>	83.8	86.4
MMDRF* [5]	86.5	94.4	88.3	87.3	75.7	86.8	86.5
LRRNet [18]	85.3	94.0	88.0	89.8	75.3	83.7	86.0
SegMIF [3]	85.7	93.8	92.0	<u>90.0</u>	77.6	83.8	87.1
DCINN [47]	86.4	93.8	87.4	87.2	76.7	79.0	85.2
SHIP [64]	86.5	<u>94.4</u>	87.3	88.4	75.5	83.7	86.0
Ours	<u>86.6</u>	94.5	<u>89.1</u>	88.9	76.6	87.4	87.2

Table 4. AP@0.5(%) for object detection on M³FD dataset. Bold-face: best, underline: second-best.

Methods	Unl	Car	Per	Bik	Cur	CS	GD	CC	Bu	mIoU
IR	97.1	83.0	66.3	49.1	34.0	50.9	59.8	40.4	51.9	59.2
VI	97.4	85.7	58.3	55.8	40.2	58.4	65.2	50.0	52.6	62.6
CDDFu* [63]	97.6	86.2	68.1	55.8	45.7	63.2	65.1	54.4	57.9	66.0
EMMA* [63]	97.7	86.1	67.8	57.6	<u>46.6</u>	61.8	66.9	55.6	56.3	66.3
MMDRF* [5]	97.6	86.1	<u>68.0</u>	58.2	44.3	63.7	69.0	53.8	60.0	66.8
LRRNet [18]	97.6	85.2	66.9	55.5	44.6	61.8	64.7	51.3	61.0	65.4
SegMIF [3]	97.6	84.5	67.0	56.6	43.1	59.5	69.2	52.9	57.2	65.4
DCINN [47]	97.7	86.6	67.3	57.0	42.0	59.0	67.3	54.2	58.8	65.5
SHIP [64]	97.6	85.8	67.3	56.0	45.9	62.6	64.6	52.4	54.6	65.2
Ours	97.7	<u>86.2</u>	68.9	<u>58.1</u>	46.1	<u>63.3</u>	<u>69.1</u>	<u>55.5</u>	<u>60.4</u>	67.3

Table 5. IoU(%) for semantic segmentation on MSRS dataset. Bold-face: best, underline: second-best.

mentation on the MSRS dataset [37], and the division follows [37]. Nine labels are background, bumps, color cones, guardrails, guardrails, curves, bicycles, people, car parking, and cars. We choose DeeplabV3 [4] as the backbone, and the intersection-union ratio (IoU) as the evaluation metric. During training, the epoch, batch size, optimizer, and initial learning rate during training are set to 500, 4, SGD, and 1e-3, respectively. The segmentation results are shown in Tab. 5. LKC-UNet better integrates the edge and contour information in the source image, which enhances the

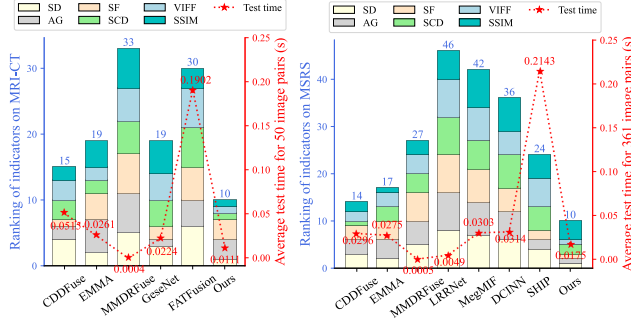


Figure 7. Comparison of fusion performance and efficiency.

model’s ability to perceive object boundaries and makes the segmentation more accurate.

4.3. Fusion efficiency

This section compares the inference time of SOTA methods on two datasets with different resolutions: 256×256 for MRI and CT images, and 640×480 for IR and VIS images in MSRS. Due to the differences in data processing and testing strategies of the different methods, we only calculate the time from calling the model to obtaining the fusion results to ensure a fair measurement. In addition, the rankings of the six metrics are presented in the form of histograms to comprehensively analyze the fusion performance and computational efficiency.

As shown in Fig. 7, our approach is slightly behind MMDRFuse and LRRNet in inference time, but they underperform in performance. In contrast, our method achieves a better trade-off between the two. It is worth noting that CDDFuse resolution decreases but inference time increases due to its two-stage testing process on medical images.

4.4. Discussion

We briefly show the visualization of the partial IVIF method on two tasks. Fig. 8 shows that training only on IR-VIS images makes it difficult to retain the complex details of medical images. Whereas training on medical images only enhances the edges and textures of the fused images, there may be problems such as retaining too much IR image noise. Therefore, it is difficult to achieve unified multi-modal image fusion by considering the data training model for only one task. Follow-up work will further consider how to balance the data differences between the two tasks to achieve a unified fusion method.

5. Conclusion

In this paper, we have analyzed the differences between medical and natural image fusion, revealing the specific fusion functions of normalization methods and demonstrating the effectiveness of large convolutional kernels. Accordingly, we can significantly enhance fusion performance using the proposed LKC-FUNet, whose basis modules com-

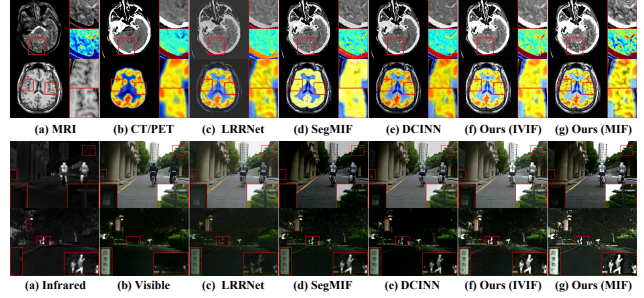


Figure 8. Visualization of IVIF methods on two tasks. The first four methods are trained on the MSRS dataset and the last column is trained only on medical images.

prise of merely two straightforward operations. Experiments show that our method achieves SOTA performance in both visual and objective evaluation metrics, and can boost the effectiveness of downstream tasks.

Acknowledgments

This work was supported by the National Natural Science Foundation of China (Nos. 62331008, 62027827, 62221005 and 62276040), the Natural Science Foundation of Chongqing (Nos. CSTB2024NSCQ-MSX0726, 2023NSCQ-LZX0045 and CSTB2022NSCQ-MSX0436), the Science and Technology Research Program of Chongqing Municipal Education Commission (No. KJQN202400507), and the Chongqing Normal University Foundation Project (No. 23XLB028).

References

- [1] Harvard medical website. <http://www.med.harvard.edu/AANLIB/home.html>. 5
- [2] Reza Azad, Ehsan Khodapanah Aghdam, Amelie Rauland, Yiwei Jia, Atlas Haddadi Avval, Afshin Bozorgpour, Sanaz Karimijafarbigloo, Joseph Paul Cohen, Ehsan Adeli, and Dorit Merhof. Medical image segmentation review: The success of u-net. *IEEE TPAMI*, PP, 2022. 4
- [3] Zhao Cai, Yong Ma, Jun Huang, Xiaoguang Mei, and Fan Fan. Correlation-guided discriminative cross-modality features network for infrared and visible image fusion. *IEEE TIM*, 2023. 7
- [4] Liang-Chieh Chen, George Papandreou, Florian Schroff, and Hartwig Adam. Rethinking atrous convolution for semantic image segmentation. *ArXiv*, abs/1706.05587, 2017. 7
- [5] Yanglin Deng, Tianyang Xu, Chunyang Cheng, Xiao-Jun Wu, and Josef Kittler. Mmdrfuse: Distilled mini-model with dynamic refresh for multi-modality image fusion. In *ACM MM*, 2024. 2, 5, 6, 7
- [6] Xiaohan Ding, Xiangyu Zhang, Jungong Han, and Guiguang Ding. Scaling up your kernels to 31x31: Revisiting large kernel design in cnns. In *CVPR*, pages 11963–11975, 2022. 3, 4
- [7] Xinjie Fan, Qifei Wang, Junjie Ke, Feng Yang, Boqing Gong, and Mingyuan Zhou. Adversarially adaptive normalization

- for single domain generalization. In *CVPR*, pages 8204–8213. IEEE, 2021. 3
- [8] Jun Fu, Weisheng Li, Jiao Du, and Liming Xu. Dsgan: A generative adversarial network based on dual-stream attention mechanism for anatomical and functional image fusion. *Inf. Sci.*, 576:484–506, 2021. 2
- [9] Dan He, Weisheng Li, Guofen Wang, Yuping Huang, and Shiqiang Liu. Mmif-inet: Multimodal medical image fusion by invertible network. *Inf. Fusion*, 114:102666, 2024. 1, 3
- [10] Han Hu, Zheng Zhang, Zhenda Xie, and Stephen Lin. Local relation networks for image recognition. In *ICCV*, pages 3464–3473, 2019. 3
- [11] Xun Huang and Serge J. Belongie. Arbitrary style transfer in real-time with adaptive instance normalization. In *ICCV*, pages 1510–1519, 2017. 3
- [12] Zhanbo Huang, Jinyuan Liu, Xin Fan, Risheng Liu, Wei Zhong, and Zhongxuan Luo. Reconet: Recurrent correction network for fast and efficient multi-modality image fusion. In *ECCV*, 2022. 2
- [13] Sergey Ioffe and Christian Szegedy. Batch normalization: Accelerating deep network training by reducing internal covariate shift. *ArXiv*, abs/1502.03167, 2015. 3
- [14] Shahid Karim, Geng Tong, Jinyang Li, Xiaochang Yu, Jia Hao, Akeel Qadir, and Yiting Yu. Mtdfusion: A multilayer triple dense network for infrared and visible image fusion. *IEEE TIM*, 73:1–17, 2024. 2
- [15] Afifa Khaled, Chao Li, Jia Ning, and Kun He. Bcn: Batch channel normalization for image classification. *ArXiv*, abs/2312.00596, 2023. 3
- [16] Sina Ghorbani Kolahi, Seyed Kamal Chaharsooghi, Toktam Khatibi, Afshin Bozorgpour, Reza Azad, Moein Heidari, Ilker Hacihaliloglu, and Dorit Merhof. Msa2net: Multi-scale adaptive attention-guided network for medical image segmentation. *arXiv preprint arXiv:2407.21640*, 2024. 4
- [17] Hui Li and Xiaojun Wu. Densefuse: A fusion approach to infrared and visible images. *IEEE TIP*, 28:2614–2623, 2018. 3
- [18] Hui Li, Tianyang Xu, Xiaojun Wu, Jiwen Lu, and Josef Kittler. Lrnnet: A novel representation learning guided fusion network for infrared and visible images. *IEEE TPAMI*, 45:11040–11052, 2023. 1, 6, 7
- [19] Jiawei Li, Jinyuan Liu, Shihua Zhou, Qiang Zhang, and Nikola Kirilov Kasabov. Learning a coordinated network for detail-refinement multiexposure image fusion. *IEEE TCSVT*, 33:713–727, 2023. 1
- [20] Jiawei Li, Jinyuan Liu, Shihua Zhou, Qiang Zhang, and Nikola K Kasabov. Gesenet: A general semantic-guided network with couple mask ensemble for medical image fusion. *IEEE TNNLS*, 2023. 5, 6
- [21] Xiaoling Li, Yanfeng Li, Houjin Chen, Yahui Peng, and Pan Pan. Ccafusion: Cross-modal coordinate attention network for infrared and visible image fusion. *IEEE TCSVT*, 34:866–881, 2024. 2
- [22] Yuxuan Li, Xiang Li, Yimain Dai, Qibin Hou, Li Liu, Yongxiang Liu, Ming-Ming Cheng, and Jian Yang. Lsknet: A foundation lightweight backbone for remote sensing. *IJCV*, pages 1–22, 2024. 3
- [23] Pengwei Liang, Junjun Jiang, Xianming Liu, and Jiayi Ma. Fusion from decomposition: A self-supervised decomposition approach for image fusion. In *ECCV*, 2022. 1
- [24] Jinyuan Liu, Runji Lin, Guanyao Wu, Risheng Liu, Zhongxuan Luo, and Xin Fan. Coconet: Coupled contrastive learning network with multi-level feature ensemble for multi-modality image fusion. *IJCV*, 132:1748–1775, 2022. 1, 3
- [25] Jinyuan Liu, Zhu Liu, Guanyao Wu, Long Ma, Risheng Liu, Wei Zhong, Zhongxuan Luo, and Xin-Yue Fan. Multi-interactive feature learning and a full-time multi-modality benchmark for image fusion and segmentation. In *ICCV*, pages 8081–8090, 2023. 1, 2, 3, 6
- [26] Min Liu, Yubin Han, Jiazheng Wang, Can Wang, Yaonan Wang, and Erik Meijering. Lskanet: Long strip kernel attention network for robotic surgical scene segmentation. *IEEE TMI*, 2023. 3
- [27] Risheng Liu, Zhu Liu, Jinyuan Liu, and Xin Fan. Searching a hierarchically aggregated fusion architecture for fast multi-modality image fusion. In *ACM MM*, 2021. 1
- [28] Shiwei Liu, Tianlong Chen, Xiaohan Chen, Xuxi Chen, Qiao Xiao, Boqian Wu, Tommi Kärkkäinen, Mykola Pechenizkiy, Decebal Mocanu, and Zhangyang Wang. More convnets in the 2020s: Scaling up kernels beyond 51x51 using sparsity. *arXiv preprint arXiv:2207.03620*, 2022. 3
- [29] Yu Liu, Chen Yu, Juan Cheng, Z. Jane Wang, and Xun Chen. Mm-net: A mixformer-based multi-scale network for anatomical and functional image fusion. *IEEE TIP*, 33:2197–2212, 2024. 1
- [30] Zhuang Liu, Hanzi Mao, Chao-Yuan Wu, Christoph Feichtenhofer, Trevor Darrell, and Saining Xie. A convnet for the 2020s. In *CVPR*, pages 11976–11986, 2022. 3
- [31] Jiayi Ma, Yong Ma, and Chang Li. Infrared and visible image fusion methods and applications: A survey. *Inf. Fusion*, 45:153–178, 2019. 5
- [32] Jiayi Ma, Wei Yu, Pengwei Liang, Chang Li, and Junjun Jiang. Fusiongan: A generative adversarial network for infrared and visible image fusion. *Inf. Fusion*, 48:11–26, 2019. 1, 3
- [33] Jiayi Ma, Linfeng Tang, Fan Fan, Jun Huang, Xiaoguang Mei, and Yong Ma. Swinfusion: Cross-domain long-range learning for general image fusion via swin transformer. *IEEE/CAA Journal of Automatica Sinica*, 9:1200–1217, 2022. 2, 3
- [34] Pan Mu, Guanyao Wu, Jinyuan Liu, Yuduo Zhang, Xin Fan, and Risheng Liu. Learning to search a lightweight generalized network for medical image fusion. *IEEE TCSVT*, 34:5921–5934, 2024. 1
- [35] Olaf Ronneberger, Philipp Fischer, and Thomas Brox. U-net: Convolutional networks for biomedical image segmentation. In *Medical image computing and computer-assisted intervention—MICCAI 2015: 18th international conference, Munich, Germany, October 5–9, 2015, proceedings, part III 18*, pages 234–241. Springer, 2015. 2
- [36] Ivan Skorokhodov and Mohamed Elhoseiny. Class normalization for (continual)? generalized zero-shot learning. In *ICLR*, 2021. 3

- [37] Linfeng Tang, Jiteng Yuan, Haotong Zhang, Xingyu Jiang, and Jiayi Ma. Piafusion: A progressive infrared and visible image fusion network based on illumination aware. *Inf. Fusion*, 83-84:79–92, 2022. 6, 7
- [38] Linfeng Tang, Yuxin Deng, Xunpeng Yi, Qinglong Yan, Yixuan Yuan, and Jiayi Ma. Drmf: Degradation-robust multi-modal image fusion via composable diffusion prior. In *ACM MM*, 2024. 1, 3
- [39] Wei Tang and Fazhi He. Fatfusion: A functional-anatomical transformer for medical image fusion. *Inf. Process. Manag.*, 61:103687, 2024. 5, 6
- [40] Wei Tang, Fazhi He, Y. Liu, and Yansong Duan. Matr: Multimodal medical image fusion via multiscale adaptive transformer. *IEEE TIP*, 31:5134–5149, 2022. 1
- [41] Wei Tang, Fazhi He, and Y. Liu. Ydtr: Infrared and visible image fusion via y-shape dynamic transformer. *IEEE TMM*, 25:5413–5428, 2023. 3
- [42] Alexander Toet. The tno multiband image data collection. *Data in Brief*, 15:249–251, 2017. 6, 7
- [43] Ultralytics. ultralytics/yolov5: v7.0 - YOLOv5 SOTA Realtime Instance Segmentation. <https://github.com/ultralytics/yolov5.com>, 2022. 6
- [44] Dmitry Ulyanov, Andrea Vedaldi, and Victor S. Lempitsky. Instance normalization: The missing ingredient for fast stylization. *ArXiv*, abs/1607.08022, 2016. 3
- [45] Di Wang, Jinyuan Liu, Risheng Liu, and Xin Fan. An interactively reinforced paradigm for joint infrared-visible image fusion and saliency object detection. *Inf. Fusion*, 98:101828, 2023. 3
- [46] Haonan Wang, Peng Cao, Jiaqi Wang, and Osmar R Zaiane. Uctransnet: rethinking the skip connections in u-net from a channel-wise perspective with transformer. In *AAAI*, pages 2441–2449, 2022. 4
- [47] Wu Wang, Liang-Jian Deng, Ran Ran, and Gemine Vivone. A general paradigm with detail-preserving conditional invertible network for image fusion. *IJCV*, 132(4):1029–1054, 2024. 1, 6, 7
- [48] Zhou Wang, Alan C Bovik, Hamid R Sheikh, and Eero P Simoncelli. Image quality assessment: from error visibility to structural similarity. *IEEE TIP*, 13(4):600–612, 2004. 5
- [49] Yuxin Wu and Kaiming He. Group normalization. *IJCV*, 128:742–755, 2018. 3
- [50] Han Xu and Jiayi Ma. Emfusion: An unsupervised enhanced medical image fusion network. *Inf. Fusion*, 76:177–186, 2021. 1, 3
- [51] Han Xu, Jiayi Ma, Junjun Jiang, Xiaojie Guo, and Haibin Ling. U2fusion: A unified unsupervised image fusion network. *IEEE TPAMI*, 44:502–518, 2020. 1
- [52] Han Xu, Jiteng Yuan, and Jiayi Ma. Murf: Mutually reinforcing multi-modal image registration and fusion. *IEEE TPAMI*, 45:12148–12166, 2023. 1
- [53] Jun Yue, Leyuan Fang, Shaobo Xia, Yue Deng, and Jiayi Ma. Dif-fusion: Toward high color fidelity in infrared and visible image fusion with diffusion models. *IEEE TIP*, 32:5705–5720, 2023. 3
- [54] Hao Zhang and Jiayi Ma. Sdnet: A versatile squeeze-and-decomposition network for real-time image fusion. *IJCV*, 129:2761–2785, 2021. 2
- [55] Hao Zhang, Xuhui Zuo, Huabing Zhou, Tao Lu, and Jiayi Ma. A robust mutual-reinforcing framework for 3d multi-modal medical image fusion based on visual-semantic consistency. In *AAAI*, 2024. 1, 3
- [56] Xingchen Zhang and Y. Demiris. Visible and infrared image fusion using deep learning. *IEEE TPAMI*, 45:10535–10554, 2023. 1
- [57] Yu Zhang, Yu Liu, Peng Sun, Han Yan, Xiaolin Zhao, and Li Zhang. Ifcnn: A general image fusion framework based on convolutional neural network. *Inf. Fusion*, 54:99–118, 2020. 2, 3
- [58] Ying Zhang, Ren qi Nie, Jinde Cao, and Chaozhen Ma. Self-supervised fusion for multi-modal medical images via contrastive auto-encoding and convolutional information exchange. *IEEE Computational Intelligence Magazine*, 18:68–80, 2023. 1, 3
- [59] Wenda Zhao, Shigeng Xie, Fan Zhao, You He, and Huchuan Lu. Metafusion: Infrared and visible image fusion via meta-feature embedding from object detection. In *CVPR*, pages 13955–13965. IEEE, 2023. 1, 3
- [60] Zixiang Zhao, Hao Bai, Jiangshe Zhang, Yulun Zhang, Shuang Xu, Zudi Lin, Radu Timofte, and Luc Van Gool. Target-aware dual adversarial learning and a multi-scenario multi-modality benchmark to fuse infrared and visible for object detection. In *CVPR*, pages 5792–5801. IEEE, 2022. 1, 3, 6, 7
- [61] Zixiang Zhao, Hao Bai, Jiangshe Zhang, Yulun Zhang, Shuang Xu, Zudi Lin, Radu Timofte, and Luc Van Gool. Cddfuse: Correlation-driven dual-branch feature decomposition for multi-modality image fusion. In *CVPR*, pages 5906–5916. IEEE, 2023. 1, 2, 3, 5, 6, 7
- [62] Zixiang Zhao, Hao Bai, Yuanzhi Zhu, Jianshe Zhang, Shuang Xu, Yulun Zhang, K. Zhang, Deyu Meng, Radu Timofte, and Luc Van Gool. Ddfm: Denoising diffusion model for multi-modality image fusion. In *ICCV*, pages 8048–8059, 2023. 3
- [63] Zixiang Zhao, Haowen Bai, Jianshe Zhang, Yulun Zhang, Kai Zhang, Shuang Xu, Dongdong Chen, Radu Timofte, and Luc Van Gool. Equivariant multi-modality image fusion. In *CVPR*, pages 25912–25921. IEEE, 2024. 1, 2, 3, 5, 6, 7
- [64] Naishan Zheng, Man Zhou, Jie Huang, Junming Hou, Haoying Li, Yuan Xu, and Feng Zhao. Probing synergistic high-order interaction in infrared and visible image fusion. In *CVPR*, pages 26374–26385. IEEE, 2024. 1, 6, 7
- [65] Pengfei Zhu, Yang Sun, Bing Cao, and Qinghua Hu. Task-customized mixture of adapters for general image fusion. In *CVPR*, pages 7099–7108. IEEE, 2024. 2